Published in final edited form as:
IEEE Trans Inf Technol Biomed. 2008 May ; 12(3): 328–334.

Unifying Statistical Classification and Geodesic Active Regions for Segmentation of Cardiac MRI

Jenny Folkesson, **Eigil Samset**, **Raymond Y. Kwong**, and **Carl-Fredrik Westin [Member, IEEE]**

J. Folkesson is with the Laboratory of Mathematics in Imaging (LMI), Department of Radiology, Brigham and Women's Hospital, Harvard Medical School, Boston, MA 02115 USA. She is also with the Department of Computer Science (DIKU), University of Copenhagen, DK-1017 Copenhagen, Denmark (jenny@bwh.harvard.edu)

E. Samset is with the Surgical Planning Laboratory, Brigham and Women's Hospital, Boston, MA 02115 USA (samset@bwh.harvard.edu)

R. Y. Kwong is with the Cardiovascular Division, Department of Medicine, Brigham and Women's Hospital, Boston, MA 02115, USA

C.-F. Westin is with the Laboratory of Mathematics in Imaging (LMI), Department of Radiology, Brigham and Women's Hospital, Harvard Medical School, Boston, MA 02115 USA (westin@bwhharvardedu)

Abstract

This paper presents a segmentation method that extends geodesic active region methods by the incorporation of a statistical classifier trained using feature selection. The classifier provides class probability maps based on class representative local features, and the geodesic active region formulation enables the partitioning of the image according to the region information. We demonstrate automatic segmentation results of the myocardium in cardiac late gadolinium-enhanced magnetic resonance imaging (CE-MRI) data using coupled level set curve evolutions, in which the classifier is incorporated both from a region term and from a shape term from particle filtering. The results show potential for clinical studies of scar tissue in late CE-MRI data.

Keywords

Cardiac magnetic resonance imaging; geodesic active regions; image segmentation; *k*NN classification

I. Introduction

ATRIAL fibrillation is a disorder found in about 2.2 million Americans, and about 15% of strokes occur in people with the disorder. Ventricular arrhythmias are the major cause of the more than 350,000 sudden cardiac deaths annually in the United States [1]. Catheter ablation of paroxysmal atrial fibrillation has emerged as a first line effective therapy that has the potential to prevent arrhythmia recurrences and improve quality of life. With increasing clinical acceptance and experience, catheter ablation of ventricular arrythmia has been increasingly used and can potentially reduce the need for implanted defibrillators.

Catheter ablation involves the selective destruction of the cardiac tissue responsible for the initiation and maintenance of arrhythmias via percutaneously placed catheters. Currently, cardiac and peripheral vascular interventions are typically guided by fluoroscopic X-ray. This imaging modality yields only limited anatomic information, uses ionizing radiation,

and iodine-based contrast agents are necessary to visualize the vessels. The use of cardiac late gadolinium-enhanced magnetic resonance imaging (CE-MRI) in such procedures eliminates the concerns of both exposure and contrast, and enables the visualization of areas of myocardial scar that contain the arrhythmia substrate [2]. Delineations of scar tissue can be useful both in preoperative MRI registered to intraoperative imaging during ablation, and in clinical studies of myocardial scar and its impact on cardiac disorders [3].

With sufficient tissue contrast and signal-to-noise ratio of the current CE-MRI technique, accurate intensity-based delineation of the scar extent is possible if myocardial segmentation can be accurately performed. Currently, clinical analysis of these types of data rely on manual labor and the segmentation of cardiac CE-MRI data is considered nontrivial [4]; hence, significant inter- and intraobserver variability can be expected. Automating the myocardium segmentation process not only eliminates the observer variability, but also relieves the cardiologists from time-consuming labor.

For an automated segmentation of the myocardium in CE-MRI, there are a number of challenges to consider besides low image contrast and noise. Irregular appearance can be found both within the myocardium where scar tissue can occur at random locations, and inside the left ventricle due to the papillary muscles. Scar tissue and protruding papillary muscles can also be a cause for missing or ambiguous boundary information between the myocardium and surrounding tissues.

Voxel-based statistical classification can deal with non-Gaussian intensity distributions, but lacks global boundary or shape information. It has been shown that adding global information can improve statistical classification results [5].

Level set methods are useful tools in image segmentation because they can change topology, and geodesic active contours enables evolution toward image boundary information while preserving regularity [6]. They have been extended to an elegant geodesic active region formalism [7] that enables a partitioning of the image according to the given region information.

Methods providing prior global shape or appearance information can be helpful when dealing with ambiguous boundary information [8]. However, global appearance models cannot capture intensity variations at random locations inside objects. Active appearance models [9] utilize a linear model of appearance by applying principal component analysis (PCA) on the intensities inside an object, something that can produce unreliable results if the intensities are not Gaussian distributed. For application to data with irregular appearance, regional statistics need to account for local and nonlinear intensity variations [10].

A. Related Work

In the literature, there are a number of shape models reported to perform well in image segmentation tasks; however, we limit the discussion to level set shape representations due to our level set framework. Leventon *et al*. [11] capture shape variations by applying PCA directly on distance function representations of objects in training data. Linear combinations of distance maps are typically not distance maps, and scale and rotation are handled implicitly in the shape model. Charpiat *et al*. [12] have generalized the distance function shape representation and modeling to a nonlinear setting. Tsai *et al*. [8] extended Leventon's model to estimate shapes with the pose parameters explicitly, where the model parameters are optimized via gradient descent using regional intensity statistics. The method does not require point correspondences during training, and the region-based optimization framework is quite general and could be extended to incorporate other features than intensity. The method has been extended to a mutual-information-driven shape estimation, which makes

no explicit assumptions on the class intensity distributions by estimating them using Parzen windowing [13]. However, PCA-based shape inference allows only combinations of shape variations found in the training data and cannot capture previously unseen fine details in a test image. Huang *et al*. use a distance map shape representation, and employ PCA to capture variations in shape and appearance in their registration-based segmentation that efficiently segments tagged cardiac MRI. However, a global linear model of appearance may be unreliable if the intensities are not normally distributed, and the model fit may be impaired by local intensity variations.

Rousson and Paragios [14] have developed a level-set-based shape model by finding a mean distance function from a set of aligned training distance maps in a maximum-likelihood sense. This mean shape is constrained to be a level set representation, and the variability at each grid location is taken into account. A level set function is then evolved that becomes optimal when it is a rigid transformation of the prior shape model. Paragios *et al*. [15] have also developed a geodesic active region method for myocardium segmentation with a region term derived by assuming separable Gaussian class intensity distributions. Cremers *et al*. [16] adopted the distance function shape representation and introduced a dynamic labeling in a Chan–Vese segmentation framework that can handle occlusions but assumes intensity homogeneity.

Pichon *et al*. [17] developed a level set segmentation method in which the contour grows toward a maximum *a posteriori* region. Parzen windows are employed for unsupervised estimation of intensity probability density functions. Parzen windowing is not restricted to normal intensity distributions; however, the method does not include shape information, and is semiautomatic. It is restricted to region growing, which might not be ideal when coupled contours are interacting.

Zeng *et al*. segment brain MRI data using level sets evolving toward locations with high probabilities of being tissue boundaries assuming Gaussian within tissue intensity distributions combined with a strong coupling force [18].

B. Overview of the Presented Work

We propose to incorporate supervised learning in terms of a statistical classifier, which makes no explicit assumptions on underlying class density functions, into a geodesic active region framework in order to deal with irregular appearance. The numerics for the two methods fit well together since all calculations are done directly at pixel level. We use a *k*NN classification framework trained by multiclass feature selection [19] in order to find suitable features for discrimination between classes. Candidate features include position, intensity smoothed on different scales, and local geometric features, as described in Sections II-A and Section II-B.

The myocardium is segmented using two coupled level sets that constrains the endo- and epicardium to remain within a certain distance relative to each other (Section II-E). A geodesic active contour term is included in order to account for boundary information (Section II-C).

Due to boundary information ambiguities in the data, we incorporate a shape term. We use a level set shape representation that fits naturally into our level set framework (Section II-D). Using a signed distance function as a shape representation could provide some tolerance to slight misalignments of the training shapes since slightly misaligned pixels in a distance map are generally correlated. This can be seen as an attempt to avoid having to solve the general correspondence problem [11], and can be advantageous for objects without well-defined anatomical landmarks, as is the case for many objects including the myocardium. Shape is

inferred by shape particle filtering [10], which, like the region term, is based on the class probability maps from classification.

For automatic myocardium segmentation, we initialize two level set representations from the shape estimates. Since these are rigid transformations of a mean shape, we allow the contours to deform locally by evolving the coupled level sets using regional information from the classification while still respecting boundary information and global shape.

II. Segmentation Method

A. Statistical Pattern Classification

In voxel-based statistical classification, each voxel is represented by *d* features in a *d*-dimensional space, and the objective is to establish decision boundaries between different classes in this feature space. Supervised methods typically establish boundaries using manually labeled training data. The *k* nearest neighbor (*k*NN) classifier determines class boundaries from the distance to the *k* nearest neighboring training data points in feature space, hence makes no assumptions on class distribution functions.

Each pixel *j* is described by a feature vector $\mathbf{u}_j$, and the posterior probability of being class ω_c is

$$P(\omega_c|\mathbf{u}_j) = \frac{k_c}{k}$$

where k_c is the number of training points of the *k* nearest neighbors with class label ω_c. The myocardium segmentation is a three-class classification problem: with the myocardium (*myo*), left ventricle (*lv*), and background (*b*). We use an approximate *k*NN classifier [20], which allows for faster computations if an error in the distance calculations is tolerated. The classifier is trained on images throughout the heart from different persons with different positioning in the scanner and different degree of scar tissue in order to cope with these variations that can occur in a test image.

B. Feature Selection

Feature selection can not only increase computational efficiency and reduce memory usage, but can also make the classification less vulnerable to the curse of dimensionality. In sequential forward selection (SFS), an initially empty feature set is expanded by iteratively adding a feature from a bank of candidate features according to the outcome of a criterion function. We apply sequential backward selection (SBS) on the features found by the SFS by iteratively excluding the least significant feature. The SFS is repeated until the classifier performance clearly has peaked, the SBS is then iterated until there is a clear performance degradation. All features are examined in every iteration, so the same feature can be selected several times that allows for an indirect weighting of important features [19]. This scheme does not guarantee a global optimum, but SFS followed by SBS examines a larger amount of possible combinations of features than, e.g., by SFS alone.

The feature selection is performed on the training data, and we use the Dice similarity coefficient (DSC) [21] as a criterion function between the classification outcome (labeled by assigning pixels to the most probable class) and manually delineated training data. For a two-class classification system, the classifier can be evaluated using the area under the receiver operating characteristics (ROC) curve [22], which evaluates the performance for all possible thresholds of the classifier. However, the myocardium is a three-class classification problem, and there are no direct extensions of the ROC for more than two classes [19]. Also,

the classifier does not need to be thresholded since both the geodesic active region term and the particle filtering use the probability map, hence soft labels, and not hard labels by thresholding. DSC measures the spatial volume overlap between two different segmentations and is defined as DSC(A, B) = $(2 \times |A \cap B|)/(|A| + |B|)$ for segmentations A and B.

The feature bank consists of the three-jet, which consists of all first-, second-, and third-order derivatives with respect to (x, y, z), and forms a basis that describes all geometric features up to third order [23]. Numerical differentiation can enhance higher spatial frequencies, an effect that increases with the order of the differentiation. Blom [24] shows that the spatial averaging in Gaussian scale–space derivatives causes a noise reduction that counteracts the noise amplification caused by differentiation. Hence, all the derivatives mentioned in this paper are Gaussian derivatives. Other candidate features are the intensity (raw and Gaussian smoothed on different scales), the position, and eigenvectors and eigenvalues of the Hessian and the structure tensor [25]. All features that involve smoothing or differentiation are evaluated on all possible combinations of six scales: 0.9, 1.5, 2.5, 3.5, 5, and 8 pixels, chosen to cover characteristics of the left ventricle and myocardium. The Hessian describes the local second-order structure:

$$\mathbf{H}(\sigma) = \begin{pmatrix} I_{xx} & I_{xy} \\ I_{yx} & I_{yy} \end{pmatrix}.$$

The structure tensor [25] examines the local first-order structure:

$$\mathbf{T}(\sigma, \sigma_T) = G_{\sigma_T} * \begin{pmatrix} I_x I_x & I_x I_y \\ I_y I_x & I_y I_y \end{pmatrix}.$$

C. Statistical Classification in Geodesic Active Regions

Caselles *et al.* [26] and Kichenassamy *et al.* [27] derived the geodesic active contour formulation for image segmentation, which is a geometric alternative of snakes [28]. A common approach to implementing the motion equation is level set methods [6], where a curve is represented implicitly by a higher dimensional function Φ.

Contour- and region-based energetic modules for evolving interfaces can be implemented using the following definitions of approximations of the Dirac and Heaviside distributions [29]:

$$\delta_\alpha(\Phi) = \begin{cases} 0, & |\Phi| < \alpha \\ (1/(2\alpha))(1+\cos(\pi\Phi/\alpha)), & |\Phi| > \alpha \end{cases}$$

$$H_\alpha(\Phi) = \begin{cases} 0, & \Phi > \alpha \\ 1, & \Phi < -\alpha \\ (1/2)(1+(\Phi/\alpha)+(1/\pi)\sin(\pi\Phi/\alpha)), & |\Phi| < \alpha \end{cases}$$

In these equations, α is the region in which the distributions are approximated, and Φ is assumed to be negative inside the contour it represents. Using these definitions, Rousson and Paragios [14] define the following active contour term:

$$\frac{d}{dt}\Phi = \delta_\alpha \operatorname{div}\left(g\left(|\nabla I|\right)\frac{\nabla\Phi}{|\nabla\Phi|}\right). \quad (1)$$

Assuming that the class probability maps from classification are conditionally independent, we seek curve evolutions that maximize the likelihood for each region [30]. This is achieved, as in [15], by minimizing

$$\begin{aligned} E\left(\Phi_I, \Phi_O\right) &= -\int\int_\Omega H_\alpha\left(\Phi_O\right)\left(1 - H_\alpha\left(\Phi_I\right)\right)\log\left(p\left(\omega_{myo}|\mathbf{u}_j\right)\right) \\ &\quad -\int\int_\Omega H_\alpha\left(\Phi_I\right)\log\left(p\left(\omega_{lv}|\mathbf{u}_j\right)\right) \\ &\quad -\int\int_\Omega\left(1 - H_\alpha\left(\Phi_O\right)\right)\log\left(p\left(\omega_b|\mathbf{u}_j\right)\right) \end{aligned}$$

where Φ_I and Φ_O represent the endo- and epicardium.

Using calculus of variations and Greens theorem, the authors in [30] derived functional derivatives of integrals along contours and over regions, which results in the following level set evolution equations [15] for the inner and outer contours:

$$\frac{d}{dt}\Phi_I = -\delta_\alpha\left(\Phi_I\right)\log\frac{p\left(\omega_{lv}|\mathbf{u}_j\right)}{p\left(\omega_{myo}|\mathbf{u}_j\right)}|\nabla\Phi_I| \quad (2)$$

$$\frac{d}{dt}\Phi_O = -\delta_\alpha\left(\Phi_O\right)\log\frac{p\left(\omega_{myo}|\mathbf{u}_j\right)}{p\left(\omega_b|\mathbf{u}_j\right)}|\nabla\Phi_O|. \quad (3)$$

These are adaptive inflationary forces that aim to shrink or expand the contours according to the classification outcome toward maximum *a posteriori* regions. These functions assume that the contours do not overlap, something that in our framework is made highly unlikely because of the coupling and shape terms.

D. Shape Modeling

We use a distance function shape representation and a shape model that accounts for local variations by assuming a mean shape Φ_M with local degrees of shape variability σ_M. The distribution in each pixel is assumed to be Gaussian, and the mean shape is estimated from a set of aligned training shapes in a maximum-likelihood sense under the constraint that the mean shape remains a signed distance function [14].

The training shapes are aligned by finding a rigid transform ($\mathbf{A} = T, \theta, s$) with respect to translation, rotation, and scale. The optimization criterion is the sum of squared differences between the source shape $\mathscr{S}$ and a target shape $\mathscr{T}$:

$$E\left(\mathbf{A}\right) = \int\int_\Omega\left(\Phi_{\mathscr{T}}\left(x, y\right) - \Phi_{\mathscr{S}}\left(\mathbf{A}\left(x, y\right)\right)\right)^2 dx\, dy$$

and shape alignment can be achieved using gradient descent by keeping the initial pose of one shape and align the remaining shapes to it. For more details, see [14] and references

therein. We constrain the shapes for the epi- and endocardium in an image to have the same pose parameters since they are closely connected.

1) Shape Particle Filtering—In a test image, we wish to make region-based shape inference based on the class probability maps. This can be realized in a variety of ways: we use shape particle filtering as in [10] since the method has demonstrated accurate results for shape inference based on *k*NN classification. The particle filtering does not easily get trapped in local maxima nor does it need initialization close to optimal solution. We use shape particle filtering to determine the best transformation of the mean shape model given the appearance model, which in our case is the *k*NN classification. A set of $f = 1, \ldots, N$ myocardium shape hypotheses (particles) are sampled randomly relative to translation, rotation, and scale variations in the training data. Each hypothesis is associated with an image labeling that is compared to the label probability maps from classification. Particles are weighted by these likelihood terms for each region

$$W = \exp\left[\frac{c}{m}\sum_{j=1}^{m}\log p\left(\mathbf{u}_j|\omega_c\right)\right]$$

where *c* is a constant controlling the randomness of the process and *m* is the number of pixels inside the template [10]. A new set of *N* hypotheses are generated from the current set by random sampling proportional to the weights W_f and random perturbation of duplicate particles, so that successful particles will multiply while unlikely shapes will vanish. This resampling is repeated until convergence to the maximum-likelihood solution, which is when the change of the strongest local mode of the particle distribution becomes negligible.

Using particle filtering we find the optimal rigid transformation of the mean shape model [annotated $\Phi_{M,i}(A_i)$] given the classification of a test image. In the evolution we include a shape term that evolves toward the inferred shape weighted by the shape variability; hence, the shape term is less influential in locations with large prior shape variability [14]:

$$\frac{d}{dt}\Phi_i = -H_\alpha\left(\Phi_i\right)\frac{\Phi_i - \Phi_{M,i}\left(A_i\right)}{\sigma^2_{M,i}\left(A_i\right)}. \quad (4)$$

E. Coupling Force

The distance between the epi- and endocardial contours is approximately constant; therefore, we introduce a coupling force that respects this anatomical constraint. The distance between the contours can be found with little computational expense from the distance functions. In [18], a coupling force is designed to slow down and eventually stop the evolution if the contours move too far away from each other given a predefined allowed distance. In [15], the coupling forces are ±1 when distances between contours are outside the allowed range and 0 otherwise.

We design a coupling force that takes advantage of prior information by calculating the distance between the epi- and endocardial contours for all contour points in the training data. We let the coupling force *h* be inactive in the interval of the average distance plus/minus half a standard deviation. Outside that range, the magnitude of the force increases as a Gaussian function with variance proportional to that of the training data, as can be seen in Fig. 1. The coupling terms for the inner and outer contour are described by

$$\frac{d}{dt}\Phi_I = \delta_\alpha(\Phi_I)(-h(-\Phi_O))|\nabla\Phi_I| \quad (5)$$

$$\frac{d}{dt}\Phi_O = \delta_\alpha(\Phi_O)(h(\Phi_I))|\nabla\Phi_O|. \quad (6)$$

When the distance between the endo- and epicardial contours are within the normal range, the coupling terms are passive, and outside that range, these forces will act as attraction/repellation between the contours when they are too far away/close to each other. In total, the curve evolution criterion for the inner contour is

$$\begin{aligned}\frac{d}{dt}\Phi_I = {} & \lambda_1\delta_\alpha \operatorname{div}\left(g(|\nabla I|)\frac{\nabla\Phi}{|\nabla\Phi|}\right) \\ & - \lambda_2\delta_\alpha(\Phi_I)\log\frac{p(\omega_{lv}|\mathbf{u})}{p(\omega_{myo}|\mathbf{u})}|\nabla\Phi_I| \\ & - \lambda_3 H_\alpha(\Phi_I)\frac{\Phi_I\Phi_{M,i}(A)}{\sigma^2_{m,i}(A)} \\ & + \lambda_4\delta_\alpha(\Phi_I)(\\ & - h(-\Phi_O))|\nabla\Phi_I|\end{aligned}$$

where the terms on the right-hand side are the boundary term, region term from classification, shape from classification, and coupling force. The evolution for the outer contour can be found in the same manner from (1), (3), (4), and (6).

The contours are initialized from the shape term, which is restricted to a rigid transformation of the mean shape from the training phase. These initial contours are typically fairly close to convergence, and the evolution will adjust the contours for local boundary and region information while preserving contour regularity and respecting inferred global shape.

III. Experimental Results

A. Data Set

CE-MRI short-axis data were acquired as in [3] using a 1.5 T cardiovascular magnetic resonance (CMR) system (Signa CV/*i*, GE Healthcare, USA), with late gadolinium enhancement (LGE) imaging (T_R/T_E 4.8/1.3 ms, T_I 200–300 ms) for myocardial scar. An inversion-recovery sequence for LGE was used starting 15 min after cumulative 0.15 mmol/kg dose of gadolinium-DPTA. The in-plane resolution was 1.5 mm × 2 mm with thickness of 8 mm. Epicardial and endocardial boundaries were manually outlined. Example slices and manual segmentations can be seen in Figs. 2 and 3. The data set consists of 11 patients, and we use 57 slices from 7 of them for training the method and 30 slices from 4 patients for evaluation.

B. Selected Features

After feature selection on the training data, the feature set consists of the following features in decreasing significance: the position, the intensity smoothed on scales 5 and 8, I_y on scales 5 and 8 (selected twice), I_{yy} on scales 5 and 8, I_x on scales 5 and 8, eigenvalues of the structure tensor, **T**(8, 8), eigenvalues of the Hessian [**H**(3.5) and **H**(8)], I_{yyy} on scales 5 and 8, I_{xy} on scales 2.5 and 3.5, eigenvalues of **T**(0.9, 1.5), **T**(2.5, 0.9), **T**(1.5, 0.9) (selected

trice), **T**(5, 1.5), and **T**(8, 5), I_{xyy} on scales 5 and 8, eigenvalues of **T**(5, 0.9), and **T**(3.5, 0.9). It can be noted that the original image intensity information is never selected as a feature, and that among the most significant features, both first- and second-order structure on high scales are predominant. Eigenvalues of the structure tensor are selected several times; hence, smoothed low-scale first-order structure is useful for discrimination between classes. The eigenvectors are not selected, which could be related to the changes in gradient direction around the myocardium contours. The features are normalized prior to classification.

C. Segmentation Evaluation

The automatic segmentation method is evaluated by comparison with manual segmentation by cardiologists. Catheter ablation involves sensing the heart walls; therefore, we evaluate a distance measure, the mean point to curve distance. In clinical studies, the percent area of the myocardium covered by scar tissue is a biomarker for coronary artery disease, and therefore, we also evaluate volume overlap using DSC. Example images along with manual and automatic segmentations and classification results can be seen in Fig. 2 and Fig. 3.

The segmentation failed to converge for 2 of the 30 test images due to inferior image quality and the extent to which scar tissue covers the myocardium. This could be the result of the limited amount of training data and the large appearance variations in the data. For the remaining 28 images, the results are presented in Table I for the classification, shape estimation, and the automatic segmentation. As can be seen in the figures and the table, the classification alone is not sufficient for a reliable segmentation. The incorporation of the classification-based shape estimate clearly improves the performance, and is used as the initialization for the curve evolution as in (7). The shape is a rigid transformation of the mean shape, so local adjustments of the shape to the image information needs to be incorporated. The evolution allows for such local adaptation of the mean shapes given region and boundary image information. Once the evolution has converged, there is a significant improvement compared to the shape estimate both in terms of DSC ($p = 0.0004$) and distance to contour d ($p = 0.015$).

In order to evaluate the influence of the region term on the final segmentation, we ran the experiments in the same way only without this term. This resulted in a significant decrease of DSC to 0.77 and an increase in the distance to contour, $d = 1.48$. Leaving out the boundary term lead to a small performance drop for the DSC (DSC = 0.78, $d = 1.44$). Leaving out the coupling force also lead to a small performance deterioration (DSC = 0.78, $d = 1.49$). Leaving out the shape term lead to the most striking performance degradation with DSC = 0.71 and $d = 2.84$; however, this is still an improvement compared to the classification on its own. Hence, the shape term is the most important term, which is most likely a product of the missing or ambiguous boundary information in the data, followed by the region term. The statistical classification contributes greatly to the results since it is incorporated both in the region term, and in the region-based shape inference. We did not attempt to substitute the region term with a Gaussian mixture model based on the intensities as in [15] since the classes cannot be discriminated using their intensity properties alone.

The inclusion of different information-driven terms can enhance the performance of the segmentation method. Still, selecting the parameters $\lambda_1, \ldots, \lambda_4$ is an issue. Based on our experiments, the shape is the most important term due to the ambiguous boundary information in the data, and we set $\lambda_3 = 0.2$. The region term is also important, and $\lambda_2 = 0.15$. The coupling force is a soft to hard constraint, and $\lambda_4 = 0.25$, and the boundary term contributes to some extent to the performance when there is strong gradients close to the contours, $\lambda_1 = 0.25$.

IV. Summary And Discussion

Spreeuwers and Breeuwer [31] segmented the myocardium semiautomatically using coupled active contours guided by intensity profiles in the normal direction of each node. They report a point to contour distance of 1.5 pixels and an intraobserver variability of 1 pixel, evaluated on eight slices from two test subjects in cine short-axis MRI data. de Bruijne and Nielsen [10] have presented an automatic segmentation method using shape particle filtering based on point distribution models (PDMs) that require point correspondences during the training phase. The method is evaluated on a data set consisting of 14 short-axis end-diastolic cardiac MRI slices with manually placed landmarks on the epi- and endocardial contour, with similar results (mean distance to contour 1.1 ± 0.3 pixels). Stegmann *et al*. [32] use an active appearance model approach to segment perfusion cardiac MRI in 4-D, and demonstrate results of 1.3 ± 0.4 pixels mean point to curve distance on the left and right ventricle combined. Our results in terms of distance to contour (1.4 ± 0.5 pixels) for the left ventricle are comparable to the results in [31] though our method is fully automatic. Our results are similar to those of Stegmann *et al*.; however, our method does not require point correspondence during training. The relatively higher distance of our method compared to [10] can be related to the ambiguous image information, in particular the enhanced scar tissue, in CE-MRI data, making the images difficult to delineate even for a trained human expert. Though we have no inter- or intraobserver data, we suspect that there are substantial variations in these delineations. Still, the evaluated data set shows as good agreement with gold standard segmentations as can be expected given the possible variations in these delineations, and future work involves evaluating the potential of the fraction of the myocardium covered by scar tissue obtained by the automatic algorithm as a potential predictive biomarker for coronary artery disease, as is done by manual analysis in [3].

Due to the large distance between slices, we focus on a 2-D description of the segmentation method in this paper, but the method can be extended to 3-D and it can be adapted to other image segmentation problems provided there is sufficient labeled training data.

In this paper, we use particle filtering for shape inference based on probability maps from classification, which demonstrates good performance and is independent of initialization. But any region-based shape inference method could be incorporated; for instance, it could be interesting to compare the performance of a gradient descent approach such as in [13], which could be adjusted to incorporate class probability maps as regional information.

If the myocardium is in a different position than described in the training set, the location feature might not contribute to the classifier performance. In order to adjust the segmentation method to become more robust to variations in myocardium location, one could redo the classification after shape inference, using the location of the inferred shape for an adjustment of the position feature. This might improve the classification; however, the position in the image is determined to be an important feature based on the feature selection that is performed on unaligned images, so the unaligned position in the image is still a strong cue to myocardium location.

In summary, we have presented a fully automatic segmentation method that unifies statistical pattern classification and geodesic active regions by a region term and a shape estimate that are both based on *k*NN classification. The level set shape representation does not require point correspondences during the training phase and makes the registration of the training shapes less sensitive to misalignments. The feature selection ensures that suitable features given the training data are employed in the classification, and makes the method able to cope with nonlinear and local appearance variations. The method also handles missing or ambiguous boundary information due to the shape estimation. This suggests that

our automatic segmentation method may become a useful tool in image-guided interventions and clinical studies of myocardial scar using late CE-MRI.

Acknowledgments

The authors would like to thank Marleen de Bruijne of the University of Copenhagen for sharing code and insights on shape particle filtering. They also thank Ole Fogh Olsen of the IT University of Copenhagen for discussions and comments on the paper.

References

[1]. Zipes D, Wellens H. Sudden cardiac death. Circulation. 1998; 98:2334–2351. [PubMed: 9826323]

[2]. Soejima K, Stevenson W, Maisel W, Sapp J, Epstein L. Electrically unexcitable scar mapping based on pacing threshold for identification of reentry circuit isthmus. Circulation. 2002; 106:1678–83. [PubMed: 12270862]

[3]. Kwong RY, Chan AK, Brown KA, Chan CW, Reynolds HG, Tsang S, Davis RB. Impact of unrecognized myocardial scar detected by cardiac magnetic resonance imaging on event-free survival in patients presenting with signs or symptoms of coronary artery disease. Circulation. 2006; 113:2733–2743. [PubMed: 16754804]

[4]. Setser RM, Bexell DG, O'Donnell TP, Stillman AE, Lieber ML, Schoenhagen P, White RD. Quantitative assessment of myocar-dial scar in delayed enhanced magnetic resonance imaging. J. Magn. Resonance Imag. 2003; 18:434–441.

[5]. Warfield SK, Kaus M, Jolesz FA, Kikinis R. Adaptive, template moderated, spatially varying statistical classification. Med. Image Anal. 2000; 4:43–55. [PubMed: 10972320]

[6]. Osher S, Sethian J. Fronts propagating with curvature-dependent speed: Algorithms based on the Hamilton-Jacobi formulation. J. Comput. Phys. 1988; 79:12–49.

[7]. Paragios N, Deriche R. Geodesic active regions: A new framework to deal with frame artition problems in computer vision. J. Vis. Commun. Image Represent. 2002; 13:249–268.

[8]. Tsai A, Yezzi A Jr. Wells W, Tempany C, Tucker D, Fan A, Grimson WE, Willsky A. A shape-based approach to the seg mentation of medical imagery using level sets. IEEE Trans. Med. Imag. Feb; 2003 22(2):137–154.

[9]. Cootes T, Edwards G, Taylor C. Active appearance models. IEEE Trans. Pattern Anal. Mach. Intell. Jun; 2001 23(6):681–685.

[10]. de Bruijne M, Nielsen M. Shape particle filtering for image segmentation. Proc. MICCAI. 2004; 3216:168–175.

[11]. Leventon, M.; Grimson, E.; Faugeras, O. Statistical shape influence in geodesic active contour models. Proc. IEEE Conf. CVPR; Jun. 2000 p. 316-322.

[12]. Charpiat G, Faugeras O, Keriven R. Approximations shape metrics and application to shape warping and empirical shape statistics. Found. Comput. Math. Feb; 2005 5(1):1–58.

[13]. Tsai A, Wells W, Tempany C, Grimson E, Willsky A. Mutual information in coupled multi-shape model for medical image segmentation. Med. Image Anal. 2004; 8(4):429–445. [PubMed: 15567707]

[14]. Rousson M, Paragios N. Shape priors for level set representations. Proc. ECCV. 2002; II:78–92.

[15]. Paragios N, Rousson M, Ramesh V. Knowledge-based registration & segmentation of the left ventricle: A level set approach. Proc. IEEE Workshop Appl. Comput. Vis. 2002:316–322.

[16]. Cremers D, Sochen N, Schnorr C. Towards recognition-based variational segmentation using shape priors and dynamic labeling. Scale Space Theories Comput. Vis. Jun.2003 2695:388–400.

[17]. Pichon, E.; Tannenbaum, A.; Kikinis, R. A statistically based surface evolution method for medical image segmentation: Presentation and validiation. Proc. 6th Int. Conf. Med. Image Comput. Comput.-Assisted Intervention (MICCAI 2003); p. 277-284.

[18]. Zeng X, Staib LH, Schultz RT, Duncan JS. Segmentation and measurement of the cortex from 3D MR images using coupled surfaces propagation. IEEE Trans. Med. Imag. Oct; 1999 18(10): 100–111.

[19]. Folkesson J, Dam EB, Olsen OF, Pettersen PC, Christiansen C. Segmenting articular cartilage automatically using a voxel classification approach. IEEE Trans. Med. Imag. Jan; 2007 26(1): 106–115.

[20]. Arya S, Mount D, Netanyahu N, Silverman R, Wu A. An optimal algorithm for approximate nearest neighbor searching in fixed dimensions. Proc. 5th ACM-SIAM. Discrete Algorithms. 1994:573–582.

[21]. Dice L. Measures of the amount of ecologic association between species. Ecology. 1945; 26:297–302.

[22]. Jain A, Duin R, Mao J. Statistical pattern recognition: A review. IEEE Trans. Pattern Anal. Mach. Intell. Jan; 2000 22(1):4–37.

[23]. Florack, L. Ph.D. dissertation, Univ. Utrecht, Utrecht. The Netherlands: 1993. The syntactical structure of scalar images.

[24]. Blom, J. Ph.D. dissertation, Univ. Utrecht, Utrecht. The Netherlands: 1992. Topological and geometrical aspects of image structure.

[25]. Weickert, J. Anisotropic Diffusion in Image Processing. Teubner; Stuttgart, Germany: 1998.

[26]. Caselles, V.; Kimmel, R.; Sapiro, G. Geodesic active contours. Proc. Int. Conf. Comput. Vis.; 1995. p. 694-699.

[27]. Kichenassamy S, Kumar A, Olver P, Tannenbaum A, Yezzi A. Gradient flows and geometric active contour models. Proc. ICCV. 1995:810–815.

[28]. Kass M, Witkin A, Terzopoulos D. Snakes: Active contour models. Int. J. Comput. Vis. 1988; 1(4):321–331.

[29]. Zhao H-K, Chan T, Merriman B, Osher S. A variational level set approach to multiphase motion. J. Comput. Phys. 1996; 127:179–195.

[30]. Zhu SC, Yuille A. Region competition: Unifying snakes, region growing, and Bayes/MDL for multiband image segmentation. IEEE Trans. Pattern Anal. Mach. Intell. Sep; 1996 18(9):884–900.

[31]. Spreeuwers L, Breeuwer M. Detection of left ventricular and epiand endocardial borders using coupled active contours. Proc. Comput. Assisted Radiol. Surg. 2003:1147–1152.

[32]. Stegmann M, Olafsdottir H, Larsson H. Unsupervised motion compensation of multi-slice cardiac perfusion MRI. Med. Image Anal. 2005; 9(4):394–410. [PubMed: 15907391]

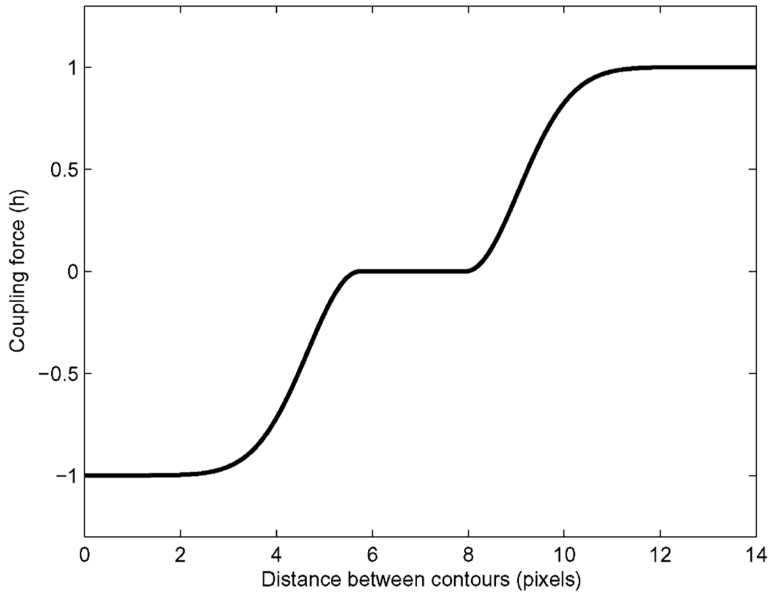

Fig. 1.
Coupling force *h* for the endocardiac and epicardiac contours.

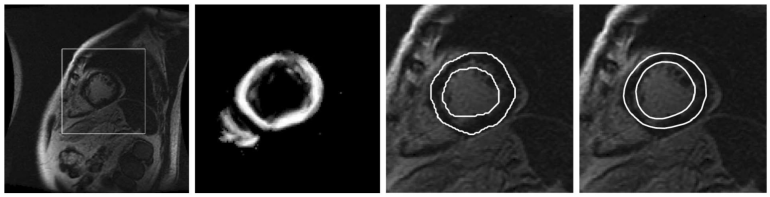

Fig. 2.
Example segmentation of the myocardium by the endo- (inner) and epi- (outer) contours. From left to right: input image where the box indicates the closeup in the remaining images, probability map for myocardium from classification, manual delineation by cardiologists, and automatic segmentation result.

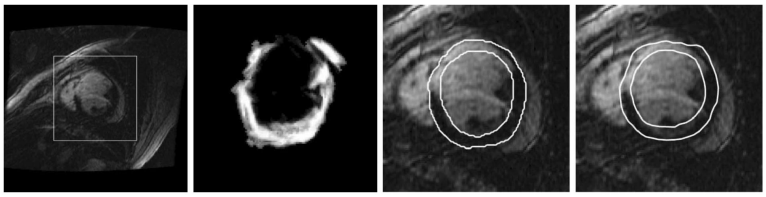

Fig. 3.
Examplesegmentation. From left to right: input image, probability map for myocardium from classification, manual delineation by cardiologists, and automatic segmentation result.

TABLE I

Results of the Segmentation Compared to Manual Segmentations Using Sensitivity, Specificity, DSC for the Myocardium, and Point Distance to Curve for the Left Ventricle (Pixels) Numbers in parenthesis are the standard deviations.

	Classification	Shape estimate	Segmentation
Sensitivity	70.2% (0.10%)	70.9% (0.08%)	75.1% (0.07%)
Specificity	99.1% (0.003%)	99.7% (0.002%)	99.7% (0.002%)
DSC	0.64 (0.11)	0.76 (0.08)	0.79 (0.07)
Distance	9.23 (6.98)	1.52 (0.51)	1.44 (0.54)